PHYSICAL REVIEW A **110**, 053102 (2024)

Evaluation of the relativistic redshift for a spaceborne optical clock

Guanhua Zhang, Jiajun Jing, Xiang Zhang, Yong Shen,[*] and Hongxin Zou[†]
Institute for Quantum Science and Technology, College of Science, National University of Defense Technology, Changsha 410073, China
and Hunan Key Laboratory of Mechanism and Technology of Quantum Information, Changsha 410073, China

(Received 11 July 2024; revised 10 September 2024; accepted 18 October 2024; published 6 November 2024)

Spaceborne optical clocks will play a significant role in the tests of fundamental physics. However, orbital motion and gravitational potential lead to the relativistic redshift (RRS), which introduces systematic errors in frequency measurements. Based on perturbation force models and orbital ephemeris data, we calculated the trajectory of the China Space Station (CSS), and evaluated the RRS of a strontium optical lattice clock aboard. The uncertainty of the RRS is estimated to be 3.3×10^{-17}, and the instability reaches 3.57×10^{-19} at 10^4 s, which is comparable to the overall uncertainty and instability of the state-of-the-art ground-based optical clock. Therefore, according to our assessment, the evaluating method for the RRS of the optical clock in the CSS is feasible and effective, and the results can serve as a reference for dynamic frequency correction of spaceborne optical clocks.

DOI: 10.1103/PhysRevA.110.053102

I. INTRODUCTION

Spaceborne optical clocks hold the promise of boosting the significance of tests of fundamental physics [1–7] and searching for physics beyond the standard model [8–12], as well as benefiting applications such as positioning, time and frequency transfer, and the accurate determination and monitoring of the geoid [13–16]. However, the variable gravitational potential in the orbit and its motion will lead to significant frequency shifts in the spaceborne optical clock. Special relativity indicates that, for an observer in an inertial frame of reference, a clock that is moving relative to them will be measured to tick slower than a clock that is at rest in their frame of reference, with a corresponding decrease in frequency (resulting in a second-order Doppler effect). This case is sometimes called special relativistic time dilation. In general relativity, gravitational redshift is the phenomenon in which electromagnetic waves or photons traveling out of a gravitational well lose energy. This loss of energy corresponds to a decrease in the wave frequency and an increase in the wavelength, known as a redshift [17]. When two clocks are located in different gravitational potentials, the clock in the higher potential measures a higher frequency compared to the clock in the lower potential. These shifts are so large that, without proper correction, the system would not work.

Several measurements of the relativistic redshift (RRS) in spaceborne microwave atomic clocks have been performed. In 1976, National Aeronautics and Space Administration (NASA) conducted the first experiment sensitive enough to measure gravitational redshift using a hydrogen maser clock on the Gravity Probe A satellite [18,19], which was positioned approximately 10000 kilometers above the earth's surface, achieving a testing accuracy of 7×10^{-5}. In 2014, Galileo satellites GSAT-0201 and GSAT-0202 of the European Global Navigation Satellite System (GNSS) Galileo, boarding a hydrogen maser, were unintentionally launched into eccentric orbits. This provides an accuracy of around 2×10^{-5} [20–22]. Atomic Clock Ensemble in Space (ACES) is a European Space Agency (ESA) mission launched in 2021 and flown on the Columbus module of the International Space Station (ISS) [23–25], which aims at improving the bound on redshift measurements to around 3×10^{-6}. The ACES payload will include the space hydrogen maser (SHM) and the cold cesium atom clock PHARAO achieving fractional frequency stability of 10^{-16}. In 2018, Litvinovd *et al.* presented an approach to probing the gravitational redshift effect, using the RadioAstron satellite [26], with an anticipated precision of 10^{-5}. For optical atomic clocks, studies evaluating the RRS of clocks have only been carried out on the ground [27–32].

In 2022, the China's Mengtian space laboratory module was launched to the China Space Station (CSS), which carries a ^{87}Sr optical clock system with the accuracy of 10^{-17} [33]. Due to the higher accuracy, the RRS is more prominent in optical clocks than microwave clocks. Particularly, for the spaceborne optical clock, the local gravitational field and instantaneous velocity vary significantly relative to those on the ground. However, the position and velocity of the CSS is provided every four minutes. Therefore, accurate real-time evaluation of the status for the CSS and the corresponding RRS is crucial for spaceborne optical clock's applications.

In this paper, based on the perturbation force models [26,34–37], we obtained the trajectory of the CSS. It is shown that, during the orbital ephemeris measurement intervals, the simulation fits well with the orbital data and the deviation exhibits as a stochastic error. Combining the orbit and gravitational field data, the RRS is calculated in real time and its Allan deviation is evaluated.

---

[*] Contact author: shenyong08@nudt.edu.cn

[†] Contact author: hxzou@nudt.edu.cn

2469-9926/2024/110(5)/053102(7)

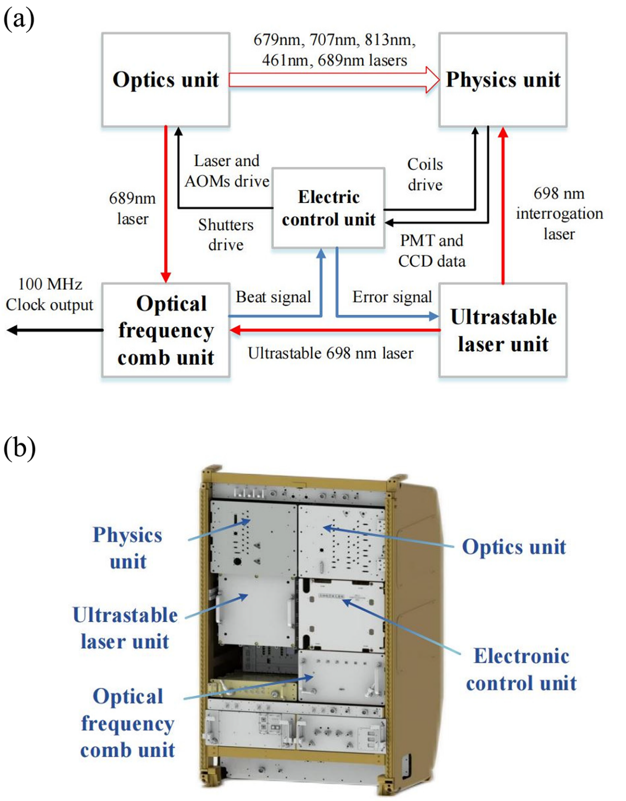

FIG. 1. The spaceborne ^{87}Sr optical clock system. (a) shows the schematic of the spaceborne ^{87}Sr optical clock system. (b) shows the rendering of the spaceborne ^{87}Sr optical clock system.

II. COMPONENTS OF THE SPACEBORNE OPTICAL CLOCK SYSTEM

The spaceborne ^{87}Sr optical clock system in the CSS, as depicted in Fig. 1, comprises five integral components: the electronic control unit, the optics unit, the physics unit, the ultrastable laser unit, and the optical frequency comb unit.

The electronic control unit serves as the central control unit of the entire system, generating drive and control signal for the optics and physics units, as well as processing the detected data.

The optics unit has lasers operating at five wavelengths: 679 nm, 707 nm, 813 nm, 461 nm, and 689 nm, along with their related optics. Figure 2 illustrates the corresponding level structure of the ^{87}Sr atom that these lasers interact with. The 461 nm laser is utilized for Zeeman slowing, the first stage cooling, and state detection. The 679 nm and 707 nm lasers are used for repumping to eliminate dark states. The 689 nm laser is employed for the second stage cooling. The 813 nm laser is used to generate the optical lattice [38].

The physics unit primarily consists of a vacuum chamber and several coils, including Zeeman slower coils, magnetic field compensation coils, and magnetooptical trap (MOT) coils. The Sr atomic beam is generated in an oven, collimated in a two-dimensional (2D) collimator, slowed in a Zeeman slower, and finally cooled and trapped in a MOT within the main vacuum chamber. Additionally, the physics unit is equipped with a CCD camera and photomultiplier tubes (PMTs) to detect the fluorescence of ^{87}Sr.

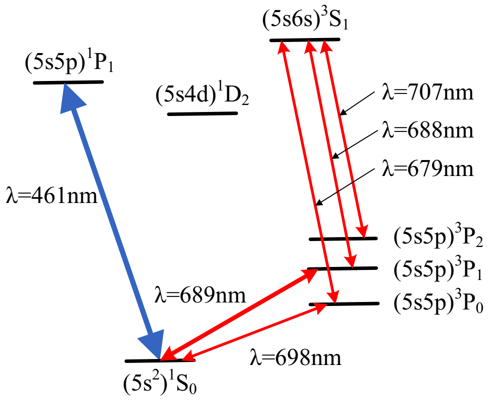

FIG. 2. The level structure used in the ^{87}Sr optical clock system (the hyperfine structure is not depicted in this figure).

In the ultrastable laser unit, a 698 nm laser is locked to an ultralow expansion (ULE) cavity. Part of this laser is sent to the physics unit for clock transition interrogation. Another part is sent to the optical frequency comb unit, serving as the frequency reference to stabilize a comb.

The optical comb unit has a repetition rate of 200 MHz, which is locked in the 698 nm ultrastable laser. Its carrier-envelope offset (CEO) frequency is locked to a hydrogen maser. Once it is locked, it also transfers the stability to the 689 nm laser via frequency offset locking.

The five units of the optical clock are housed in separate cabinets and interconnected through optical fibers and cables. Finally, when the frequency locking loop is closed, the optical comb unit outputs a 100 MHz clock signal for various applications.

III. EVALUATION OF THE GRAVITATIONAL FIELD

The RRS is closely related to the earth's gravitational field [25]. The earth is not a perfect sphere and has an uneven mass distribution. Therefore, the universal gravitational formula does not accurately describe the gravitational field of the earth. By using the spherical harmonic series, for the motion of real satellites, the gravitational potential V can be modeled as [39]

$$V(r,\phi,\lambda)=\frac{GM}{r}\left[1+\sum_{l=2}^{\infty}\sum_{m=0}^{l}\left(\frac{a}{r}\right)^{l}\bar{P}_{lm}(\sin\phi)[\bar{C}_{lm}\cos(m\lambda)+\bar{S}_{lm}\sin(m\lambda)]\right]. \tag{1}$$

Here, GM is the geocentric gravitational constant, a is the equatorial radius of the earth, r is the distance from the space station to the center of the earth, ϕ is the latitude, λ is the longitude, and $\bar{P}_{lm}(\sin\phi)$ is the associated Legendre function. $\bar{C}_{lm}, \bar{S}_{lm}$ are coefficients of the spherical functions, and vary for different earth gravitational models. l is the degree of the selected gravitational model, and m is the order of the selected gravitational model. The higher their values, the more parameters the model has, and the more precise the results obtained. The associated Legendre functions $\bar{P}_{lm}(\sin\phi)$ are shown as follows [39]:

$$\bar{P}_{(l+1)(l+1)}(x) = \bar{P}_{ll}(x)\sqrt{\frac{(2l+3)}{(l+1)(2-\delta_{0l})}(1-x^2)}, \quad (2)$$

$$\bar{P}_{(l+1)l}(x) = x\bar{P}_{ll}(x)\sqrt{2l+3}, \quad l \geqslant 1, \quad (3)$$

$$\bar{P}_{(l+1)m}(x) = x\bar{P}_{lm}(x)\sqrt{\frac{(2l+1)(2l+3)}{(l+m+1)(l-m+1)}} - \bar{P}_{(l-1)m}(x)\sqrt{\frac{(l+m)(l-m)(2l+3)}{(l+m+1)(l-m+1)(2l-1)}}, \quad (4)$$

$$\bar{P}_{00}(x) = 1, \quad \bar{P}_{10}(x) = \sqrt{3}x, \quad \bar{P}_{11}(x) = \sqrt{3(1-x^2)}. \quad (5)$$

The Earth Gravitational Model EGM2008 provides a high-resolution representation of the earth's gravitational potential. The official EGM2008 model has been publicly released by the U.S. National Geospatial-Intelligence Agency (NGA) EGM Development Team, which gives the spherical harmonic coefficients of the static earth potential needed to compute the gravitational potential at a given position [34]. The variations in EGM2008 geoid undulations compared to independent GPS or leveling values are on the order of ±5 to ±10 cm. This gravitational model is complete to spherical harmonic degree and order 2159 and contains additional coefficients up to degree 2190 and order 2159. The coefficients $\bar{C}_{lm}$ and $\bar{S}_{lm}$ can be obtained by consulting the relevant coefficient tables. In our work, we use the EGM2008 model to determine the gravitational potential, expanding the computation to the 200th order using the coefficients $\bar{C}_{lm}$ and $\bar{S}_{lm}$ from the 0th to the 200th order. This is because, from the 40th to the 100th order, the redshift and the convergence value remain within the range of 10^{-17} at this scale. Beyond the 200th order, the changes in redshift are no longer visible at this scale [25]. Therefore, the calculation at the 200th order meets our simulation requirements.

During the calculation process, it is necessary to transform between the Earth-Centered Inertial (ECI) coordinate system J2000.0 and the Earth-Centered-Earth-Fixed (ECEF) coordinate system. Since the orbit data is in the ECEF coordinate system, and the gravitational potential of the earth in Eq. (1) is expressed in the ECI coordinate system.

Assuming rotations around the x, y, and z axes by angles α, β, and θ, respectively, the rotation matrix can be expressed as

$$R_x(\alpha) = \begin{pmatrix} 1 & 0 & 0 \\ 0 & \cos\alpha & \sin\alpha \\ 0 & -\sin\alpha & \cos\alpha \end{pmatrix}, \quad (6)$$

$$R_y(\beta) = \begin{pmatrix} \cos\beta & 0 & -\sin\beta \\ 0 & 1 & 0 \\ \sin\beta & \cos\beta & 0 \end{pmatrix}, \quad (7)$$

$$R_z(\theta) = \begin{pmatrix} \cos\theta & \sin\theta & 0 \\ -\sin\theta & \cos\theta & 0 \\ 0 & 0 & 1 \end{pmatrix}. \quad (8)$$

The transformation from ECI coordinate system to ECEF coordinate system can be written as [40]

$$\boldsymbol{r}_{\mathrm{ECEF}} = R_{\mathrm{PM}}R_{\mathrm{ER}}R_{\mathrm{N}}R_{\mathrm{P}}\boldsymbol{r}_{\mathrm{ECI}}, \quad (9)$$

and

$$R_{\mathrm{P}} = R_z(-z_A)R_y(\theta_A)R_z(-\xi_A), \quad (10)$$

$$R_{\mathrm{N}} = R_x(-\varepsilon-\Delta\varepsilon)R_z(-\Delta\varphi)R_x(\varepsilon), \quad (11)$$

$$R_{\mathrm{ER}} = R_z(S_G), \quad (12)$$

$$R_{\mathrm{PM}} = R_y(-x_p)R_x(-y_p). \quad (13)$$

Here, $\boldsymbol{r}$ is the position in the coordinate system, R_{P} is the precession matrix with precession parameters (z_A, θ_A, and ξ_A), R_{N} is the nutation matrix with obliquity nutation and longitude nutation parameters ($\Delta\varepsilon$ and $\Delta\varphi$), R_{ER} is the earth rotation matrix with the Greenwich Apparent Sidereal Time S_G (the angle of the earth's rotation from the equinox of date to the Greenwich meridian), and R_{PM} is the polar motion matrix with x_p and y_p components (the angles between the pole of date and the CIO pole) [39].

IV. SIMULATION OF THE TRAJECTORY OF THE CSS

According to the China Manned Space Agency (CMSA) [41], the orbital data of the CSS has a period of approximately 1 h and 32 min. Figure 3 shows the trace of the CSS in one period, one day, and seven days, respectively. The unclosed trace of the CSS indicates that the RRS varies in different periods. For optical clocks, the typical feedback cycle is several seconds, while the orbital data of the CSS is only provided every 4 min, which is too coarse. Therefore, for precise clock comparisons, the continuous trajectory of the CSS needs to be determined.

The CSS is attracted not only by the central force of the earth, but also by the noncentral force, that is, the attraction forces of the sun and the moon, and the drag force of the atmosphere. Additionally, it is influenced by solar radiation pressure, earth and ocean tides, and so on. The perturbed equation of motion of the station is described by Newton's second law in an inertial coordinate system as [39]

$$\ddot{\boldsymbol{r}} = -\frac{GM}{|\boldsymbol{r}|^3}\boldsymbol{r} + f_1(t, \boldsymbol{r}, \dot{\boldsymbol{r}}, \boldsymbol{\sigma}), \quad (14)$$

where $\dot{\boldsymbol{r}}$ and $\ddot{\boldsymbol{r}}$ represent velocity υ and acceleration vectors of the CSS in the inertial frame, respectively, $\boldsymbol{\sigma}$ is the dynamic perturbation parameter vector. The first term represents the acceleration due to the gravitational force from the earth's center, while the second term accounts for the perturbation acceleration caused by other perturbation forces. The perturbation force models used in the simulation are listed in Table I.

With the orbital dynamics model, the trajectory of the CSS can be simulated numerically given the initial state vector of the CSS in Eq. (14). Among various numerical integration methods, the Runge-Kutta-Fehlbrg (RKF) 7(8) method is known for its high precision in calculating high-accuracy orbits. Furthermore, it is capable of adaptive step size control, which can improve computational efficiency. RKF7(8) is a

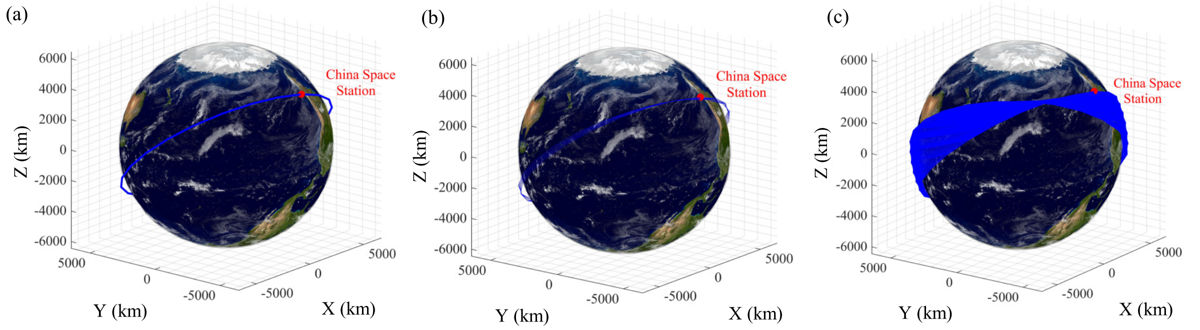

FIG. 3. (a) One-period orbit, (b) one-day orbits, and (c) seven-day orbits of the CSS in the Earth-Centred Inertial (ECI) Coordinate System. The solid blue lines are orbits, and the red dot is the initial position of the CSS.

commonly used numerical method in many areas and commercial software [40,42,43].

In a continuous simulation, we adopt the RKF7(8) method to obtain a one-day trajectory with an initial time of October 12, 2023. Figure 4 shows the deviations in position and velocity between the actual orbital data and the simulated results. Due to the limitation of perturbation force models, the simulation error will accumulate as time increases. As shown in Fig. 4, when the simulation time exceeds 8.5 h, the simulation error starts to oscillate greatly, with the period identical with the CSS orbital period. The oscillation results from the thrust of the CSS, which is not included in the model. To promote simulation accuracy, we restrict the simulation in the four-minute interval, and reset the status of the CSS with the orbital data provided by CMSA before proceeding with the next interval simulation.

With the modified method, a seven-day trajectory of the CSS is simulated. As shown in Fig. 5, the deviation between simulated results and measured orbital ephemeris data is sufficiently suppressed. Specifically, the distance deviation Δr is constrained within a range of 0.3 m, while the velocity deviation $\Delta \upsilon$ is confined within a range of 0.001 m/s. The oscillation with the same period of the CSS orbital motion still exists, but with a constant amplitude due to the reset at the beginning of each four-minute interval.

The frequency spectrum of the deviation is illustrated in Fig. 5(b). The distance deviation Δr exhibits no apparent periodic characteristics and can be considered as a random error. In terms of the deviation spectra of the elevation angle ϕ, azimuth angle λ, and velocity υ, apparent peaks exhibit harmonic frequencies of the orbital motion of the CSS. Once the data of the CSS orbit adjustment, this low-frequency noise can be sufficiently suppressed, and the residual noise is essentially white [see Fig. 5(c)]. The accuracy of the propagated orbit data obtained through the phased integration method is significantly better than that obtained from long-term numerical integration in Fig. 5. Therefore, we use the modified simulation results to calculate the RRS for the space optical clock.

TABLE I. Perturbation force models.

Perturbation Force	Model
Earth's Gravitational Field	EGM2008
Earth and Ocean Tides	IERS Conventions (2010)
Solar System bodies	DE440
Solar Radiation Pressure	Dual Cone
Atmospheric Drag	NRLMSISE-00

V. EVALUATION OF THE RELATIVISTIC REDSHIFT

In the framework of general relativity, the proper time increment τ for a clock near the earth changes according to the equation [44,45]:

$$\mathrm{d}\tau = \left(1 + \frac{V}{c^2} - \frac{\upsilon^2}{2c^2}\right)\mathrm{d}t, \tag{15}$$

where c is the speed of light in vacuum, υ is the satellite's velocity in a local ECI reference frame, V is the gravitational potential, and $\mathrm{d}t$ is the time increment in a coordinate system at rest at infinity. The second term corresponds to the gravitational redshift while the third term accounts for the second-order Doppler effect from special relativity. The ratio $\mathrm{d}\tau/\mathrm{d}t$ also equals the frequency ratio between two clocks:

$$\frac{\mathrm{d}\tau}{\mathrm{d}t} = \frac{\nu}{\nu_0}, \tag{16}$$

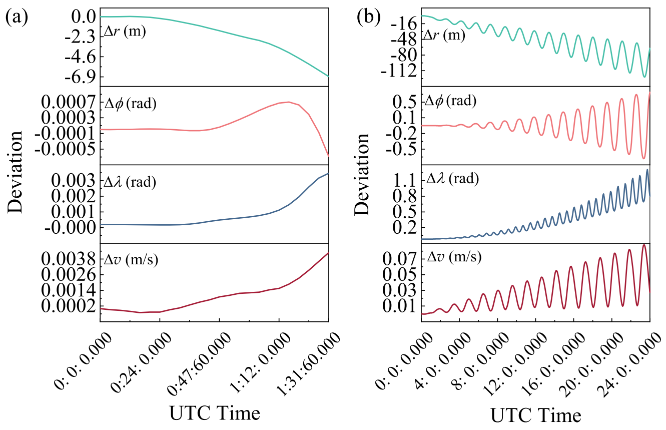

FIG. 4. Deviations in position and velocity between the actual orbital ephemeris data and the continuous simulation results. (a) shows one-period orbit data, and (b) shows one-day orbit data. r, ϕ, and λ are spherical coordinates, and υ is velocity of the space station.

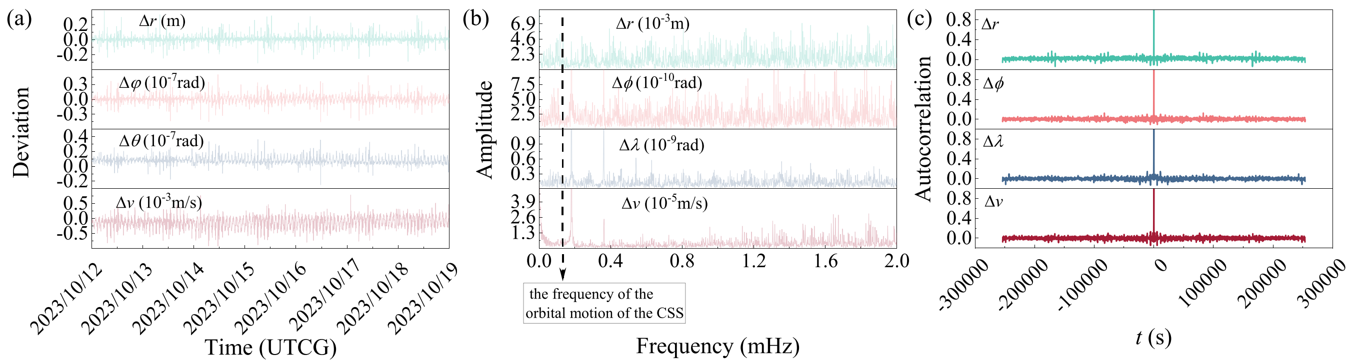

FIG. 5. Deviations in position and velocity between the actual orbital ephemeris data and the modified simulation results. (a) shows the deviations of seven-day orbit data, (b) shows the frequency spectrum of deviations within seven days, and (c) shows the autocorrelation function of the processed deviations. r, ϕ, and λ are spherical coordinates, and υ is velocity of the space station.

where ν_0 and ν are the transition frequencies of the optical clocks. We define the fractional RRS by using the fractional frequency shift between these two clocks as

$$\frac{f_{\text{RRS}}}{f} = \frac{\Delta\nu}{\nu_0} = \frac{\nu - \nu_0}{\nu_0} = \frac{\mathrm{d}\tau}{\mathrm{d}t} - 1, \tag{17}$$

where f_{RRS} is the RRS of the optical frequency f. The RRS is calculated based on Eqs. (15)–(17) and the propagated orbit of the CSS. The fractional RRS of the propagated orbits within one period, one day, and seven days are shown in Fig. 6.

In the previous studies on the RRS of ground-based atomic clocks compared to the geoid [27–30], the uncertainty of the relative gravitational redshift depends on the uncertainty of the height of the ground atomic clocks. Because on the surface of the earth $g \approx 9.8\,\text{m/s}^2$, one centimeter of orthometric height change corresponds to a fractional frequency shift $f_{\text{RRS}}/f_0 \approx 1.1 \times 10^{-18}$. Therefore, a frequency standard with an accuracy of 1×10^{-18} requires the determination of its orthometric height to an accuracy of 1 cm or better, so that the RRS correction does not degrade the accuracy of the frequency standard in its contribution to International Atomic Time (TAI). To evaluate the uncertainty and stability of the RRS of the spaceborne optical clocks, we compare the simulated results with the actual orbital ephemeris data provided by CMSA.

In the uncertainty and stability evaluations of the RRS, we consider four error sources, as follows:

$$\delta f_{\text{RRS}} = \delta f_{\text{CSS}} + \delta f_{\text{GP}} + \delta f_{\text{tide}} + \delta f_{\text{sim}}, \tag{18}$$

where δf_{RRS} is the total error, δf_{CSS} is the orbit error of CSS, δf_{tide} is tidal correction residual, δf_{GP} is the gravitational potential error, and δf_{sim} is the orbit simulation error. The orbit error of CSS is the measurement error of the actual orbit every four minutes. For the CSS, the position accuracy is about ±0.1 m [46], corresponding to a clock fractional frequency uncertainty σ_{CSS} of 1.0×10^{-17}. The gravitational potential error is related to the calculation accuracy of gravitational potential and the gravity field model EGM2008. The EGM2008 accuracy is about $\pm 0.3\,\text{m}^2/\text{s}^2$ [47], corresponding to a clock fractional frequency uncertainty σ_{GP} of 3.0×10^{-17}. The tidal correction residual is at $\pm 0.1\,\text{m}^2/\text{s}^2$ level [35,47], corresponding to a clock fractional frequency uncertainty σ_{tide} of 1.0×10^{-17}. In Eq. (18), the orbit error of CSS (δf_{CSS}), the tidal correction residual (δf_{tide}), and the gravitational potential error (δf_{GP}) are all independent systematic errors. The orbit simulation error (δf_{sim}) is the error generated when simulating the orbit during a four-minute interval. By analyzing the noise spectrum of the orbit simulation error discussed in Sec. IV, we have identified it as a stochastic error. The uncertainty index of the atomic clock typically considers the impacts brought about by systematic errors [48]. Therefore, the calculation of

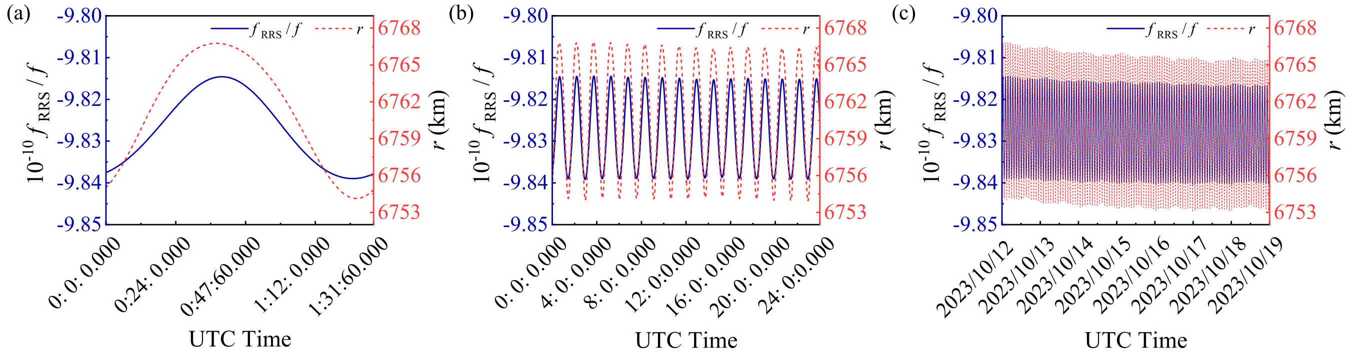

FIG. 6. The fractional relativistic redshift and the radial coordinate of the propagated orbits of CSS within (a) one period, (b) one day, and (c) seven days as functions of UTC time. The blue solid line represents fractional relativistic redshift f_{RRS}/f, and the red dashed line represents radial coordinate r of the space station.

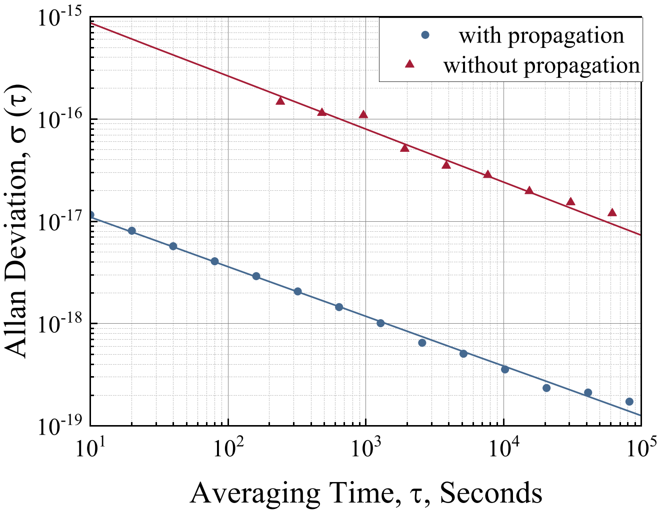

FIG. 7. The Allan deviations of the RRS. The blue dots represent the Allan deviation calculated by the actual orbit data with propagation, while the red triangles depict the Allan deviation calculated by the actual orbit data. The blue and red fitted curves represent their linear regressions, respectively.

the total uncertainty $\sigma_{\rm RRS}$ is as follows:

$$\sigma_{\rm RRS} = \sqrt{\sigma_{\rm CSS}^2 + \sigma_{\rm tide}^2 + \sigma_{\rm GP}^2} = 3.3 \times 10^{-17}. \tag{19}$$

The stability of the RRS is evaluated in two ways, as shown in Fig. 7. The Allan deviations of the statistical data with and without propagation are compared. Additionally, we performed linear regression on both types of deviations. As seen in Fig. 7, we found a significant improvement in the short-term stability and a two-order-of-magnitude improvement in the long-term stability after the orbit propagation. The instability of the RRS calculation after propagation can reach 3.57×10^{-19} at 10^4 s.

The measured absolute frequency of the clock transition in the ^{87}Sr optical lattice clock at the National Time Service Center is 429 228 004 229 872.91(18) Hz [48] with a total relative uncertainty of 5.1×10^{-17}. Based on our simulated results of the CSS, the fractional RRS is approximately 9.83×10^{-10} with an uncertainty of 3.3×10^{-17}. Our results indicate that the uncertainty of the RRS is lower than the main frequency shifts of the ground-based optical clock at NTSC. We aim to compare the frequency of the spaceborne optical clock in the CSS with that of the ground-based optical clock, which requires precise estimation and evaluation of the uncertainty and instability of the spaceborne optical clock. In this work, we enhanced the stability through orbital propagation and accurately evaluated the uncertainty. As a result, we have successfully reduced the relevant uncertainty and instability of the RRS below those of the ground-based optical clock, proving that this factor will not limit the accuracy of the frequency comparison. Therefore, the evaluation method for the RRS of the optical clock in the CSS is feasible and effective.

VI. CONCLUSION

This study utilizes the EGM2008 model to calculate the variation of gravitational potential and extrapolate the orbital ephemeris data of the CSS using perturbation models and the RKF7(8) numerical integration method. The RRS is calculated based on the simulated results of the CSS, which is around 9.8×10^{-10}. The uncertainty of the RRS is estimated to be 3.3×10^{-17}, and the instability reaches 3.57×10^{-19} at 10^4 s. The results can serve as a reference for frequency dynamic correction of spaceborne optical clocks.

This study presents an effective method for evaluating the relativistic redshift of the cold atomic clock on the China Space Sation and provides a reference for future relativistic redshift compensation. Space optical clocks play a crucial role and have broad prospects in the fields of modern science and technology such as navigation, dark matter searches, geodesy, and tests of fundamental physics. Furthermore, spaceborne optical clocks have great potential for future development. With the progress of technologies, we can foresee greater breakthroughs in spaceborne optical clocks, including longer time stability and broader applications. Moreover, spaceborne optical clocks can be combined with research in other fields, such as gravitational wave detection and the study of variations in fundamental physical constants, providing us with more precise tools to explore the universe and understand nature.

ACKNOWLEDGMENTS

This work was supported by the National Natural Science Foundation of China under Grants No. 62375284, No. 62275268, and No. 62105368, and The Science and Technology Innovation Program of Hunan Province under Grant No. 2023RC3010.

---

[1] C. W. Chou, D. B. Hume, T. Rosenband, and D. J. Wineland, Science **329**, 1630 (2010).

[2] J. Kentosh and M. Mohageg, Phys. Rev. Lett. **108**, 110801 (2012).

[3] S. Peil, S. Crane, J. L. Hanssen, T. B. Swanson, and C. R. Ekstrom, Phys. Rev. A **87**, 010102(R) (2013).

[4] P. Delva, A. Hees, and P. Wolf, Space Sci. Rev. **212**, 1385 (2017).

[5] C. Qin, Y. Tan, and C. Shao, Phys. Lett. B **820**, 136471 (2021).

[6] A. Derevianko, K. Gibble, L. Hollberg, N. R. Newbury, C. Oates, M. S. Safronova, L. C. Sinclair, and N. Yu, Quantum Sci. Technol. **7**, 044002 (2022).

[7] D. R. Gozzard, L. A. Howard, B. P. Dix-Matthews, S. F. E. Karpathakis, C. T. Gravestock, and S. W. Schediwy, Phys. Rev. Lett. **128**, 020801 (2022).

[8] K. Van Tilburg, N. Leefer, L. Bougas, and D. Budker, Phys. Rev. Lett. **115**, 011802 (2015).

[9] A. Arvanitaki, J. Huang, and K. Van Tilburg, Phys. Rev. D **91**, 015015 (2015).

[10] A. Hees, J. Guéna, M. Abgrall, S. Bize, and P. Wolf, Phys. Rev. Lett. **117**, 061301 (2016).

[11] C. Kouvaris, E. Papantonopoulos, L. Street, and L. C. R. Wijewardhana, Phys. Rev. D **104**, 103025 (2021).

[12] V. Schkolnik, D. Budker, O. Fartmann, V. Flambaum, L. Hollberg, T. Kalaydzhyan, S. Kolkowitz, M. Krutzik, A. Ludlow, N. Newbury, C. Pyrlik, L. Sinclair, Y. Stadnik, I. Tietje, J. Ye, and J. Williams, Quantum Sci. Technol. **8**, 014003 (2023).

[13] A. D. Ludlow, M. M. Boyd, J. Ye, E. Peik, and P. O. Schmidt, Rev. Mod. Phys. **87**, 637 (2015).

[14] T. E. Mehlstäubler, G. Grosche, C. Lisdat, P. O. Schmidt, and H. Denker, Rep. Prog. Phys. **81**, 064401 (2018).

[15] J. Müller, D. Dirkx, S. M. Kopeikin, G. Lion, I. Panet, G. Petit, and P. N. A. M. Visser, Space Sci. Rev. **214**, 5 (2018).

[16] J. Grotti, I. Nosske, S. B. Koller, S. Herbers, H. Denker, L. Timmen, G. Vishnyakova, G. Grosche, T. Waterholter, A. Kuhl, S. Koke, E. Benkler, M. Giunta, L. Maisenbacher, A. Matveev, S. Dörscher, R. Schwarz, A. Al-Masoudi, T. W. Hänsch, T. Udem, R. Holzwarth, and C. Lisdat, Phys. Rev. Appl. **21**, L061001 (2024).

[17] M. A. Hohensee, S. Chu, A. Peters, and H. Müller, Phys. Rev. Lett. **106**, 151102 (2011).

[18] R. F. C. Vessot and M. W. Levine, Gen. Relat. Gravit. **10**, 181 (1979).

[19] R. F. C. Vessot, M. W. Levine, E. M. Mattison, E. L. Blomberg, T. E. Hoffman, G. U. Nystrom, B. F. Farrel, R. Decher, P. B. Eby, C. R. Baugher, J. W. Watts, D. L. Teuber, and F. D. Wills, Phys. Rev. Lett. **45**, 2081 (1980).

[20] P. Delva, A. Hees, S. Bertone, E. Richard, and P. Wolf, Class. Quantum Grav. **32**, 232003 (2015).

[21] S. Herrmann, F. Finke, M. Lülf, O. Kichakova, D. Puetzfeld, D. Knickmann, M. List, B. Rievers, G. Giorgi, C. Günther, H. Dittus, R. Prieto-Cerdeira, F. Dilssner, F. Gonzalez, E. Schönemann, J. Ventura-Traveset, and C. Lämmerzahl, Phys. Rev. Lett. **121**, 231102 (2018).

[22] P. Delva, N. Puchades, E. Schönemann, F. Dilssner, C. Courde, S. Bertone, F. Gonzalez, A. Hees, C. Le Poncin-Lafitte, F. Meynadier, R. Prieto-Cerdeira, B. Sohet, J. Ventura-Traveset, and P. Wolf, Phys. Rev. Lett. **121**, 231101 (2018).

[23] L. Cacciapuoti and C. Salomon, Eur. Phys. J. Spec. Top. **172**, 57 (2009).

[24] F. Meynadier, P. Delva, C. le Poncin-Lafitte, C. Guerlin, and P. Wolf, Class. Quantum Grav. **35**, 035018 (2018).

[25] E. Savalle, C. Guerlin, P. Delva, F. Meynadier, C. le Poncin-Lafitte, and P. Wolf, Class. Quantum Grav. **36**, 245004 (2019).

[26] D. Litvinov, V. Rudenko, A. Alakoz, U. Bach, N. Bartel, A. Belonenko, K. Belousov, M. Bietenholz, A. Biriukov, R. Carman, G. Cimó, C. Courde, D. Dirkx, D. Duev, A. Filetkin, G. Granato, L. Gurvits, A. Gusev, R. Haas, G. Herold, A. Kahlon, B. Kanevsky, V. Kauts, G. Kopelyansky, A. Kovalenko, G. Kronschnabl, V. Kulagin, A. Kutkin, M. Lindqvist, J. Lovell, H. Mariey, J. McCallum, G. Molera Calvés, C. Moore, K. Moore, A. Neidhardt, C. Plötz, S. Pogrebenko, A. Pollard, N. Porayko, J. Quick, A. Smirnov, K. Sokolovsky, V. Stepanyants, J.-M. Torre, P. De Vicente, J. Yang, and M. Zakhvatkin, Phys. Lett. A **382**, 2192 (2018).

[27] N. K. Pavlis and M. A. Weiss, Metrologia **40**, 66 (2003).

[28] N. K. Pavlis and M. A. Weiss, Metrologia **54**, 535 (2017).

[29] D. Calonico, A. Cina, I. Bendea, F. Levi, L. Lorini, and A. Godone, Metrologia **44**, L44 (2007).

[30] J. Lee, J. H. Kwon, C. Y. Park, H. Kim, I.-M. Choi, J. W. Chung, and W.-K. Lee, Metrologia **61**, 015008 (2024).

[31] M. Takamoto, I. Ushijima, N. Ohmae, T. Yahagi, K. Kokado, H. Shinkai, and H. Katori, Nature Photon. **14**, 411 (2020).

[32] T. Bothwell, C. J. Kennedy, A. Aeppli, D. Kedar, J. M. Robinson, E. Oelker, A. Staron, and J. Ye, Nature (London) **602**, 420 (2022).

[33] F. Guo, W. Tan, C.-h. Zhou, J. Xia, Y.-x. Chen, T. Liang, Q. Liu, Y. Liu, D.-j. He, Y.-z. Zhou, W.-h. Wang, Y. Shen, H.-x. Zou, and H. Chang, AIP Adv. **11**, 125116 (2021).

[34] N. K. Pavlis, S. A. Holmes, S. C. Kenyon, and J. K. Factor, J. Geophys. Res. Solid Earth **117**, 2011JB008916 (2012).

[35] G. Petit and B. Luzum, The 2010 Reference Edition of the IERS Conventions, in *Reference Frames for Applications in Geosciences*, edited by Z. Altamimi and X. Collilieux (Springer, Berlin, Heidelberg, 2013), pp. 57–61.

[36] J. M. Picone, A. E. Hedin, D. P. Drob, and A. C. Aikin, J. Geophys. Res.: Space Phys. **107**, SIA 15 (2002).

[37] R. S. Park, W. M. Folkner, J. G. Williams, and D. H. Boggs, Astron J. **161**, 105 (2021).

[38] Y. Liu, W. Wang, D. He, Y. Zhou, Y. Shen, and H. Zou, Acta Phys. Sin. **72**, 171 (2023).

[39] G. Xu and Y. Xu, *GPS* (Springer, Berlin, 2007).

[40] O. Montenbruck, E. Gill, and F. Lutze, Appl. Mech. Rev. **55**, B27 (2002).

[41] C. M. S. Agency, Orbital parameters of China Space Station, https://www.cmse.gov.cn/gfgg/zgkjzgdcs/ (accessed on June 19, 2024).

[42] J. Leith and R. P. Russell, J. Astronaut. Sci. **70**, 7 (2023).

[43] J. Tang, X. Hou, and L. Liu, Adv. Space Res. **59**, 762 (2017).

[44] D. W. Sciama, Rev. Mod. Phys. **36**, 463 (1964).

[45] N. Ashby, Living Rev. Relativ. **6**, 1 (2003).

[46] S. Mingguo, G. Pengqi, L. Zhenwei, S. JianNan, D. Xue, and Z. You, Chin. Sci. Bull. **62**, 2796 (2017).

[47] W. Shen, P. Zhang, Z. Shen, R. Xu, X. Sun, M. Ashry, A. Ruby, W. Xu, K. Wu, Y. Wu, A. Ning, L. Wang, L. Li, and C. Cai, Phys. Rev. D **108**, 064031 (2023).

[48] X. Lu, F. Guo, Y. Wang, Q. Xu, C. Zhou, J. Xia, W. Wu, and H. Chang, Metrologia **60**, 015008 (2023).